NASA Contractor Report 165690

NASA-CR-165690
19810014881

STUDIES OF COMPRESSIBLE SHEAR FLOWS AND TURBULENT DRAG REDUCTION

Steven A. Orszag

CAMBRIDGE HYDRODYNAMICS, INC.
CAMBRIDGE, MASSACHUSETTS 02139

CONTRACT NAS1-15844

APRIL 1981

NASA
National Aeronautics and
Space Administration

Langley Research Center
Hampton, Virginia 23665

TABLE OF CONTENTS

	Introduction	1
1.	Analysis of Numerical Conformal Mapping (by S.A. Orszag and M. Dubiner)	2
2.	Numerical Simulation of Compressible Shear Flows on the CYBER-203 (by S. Bokhari, M. Y. Hussaini, J. J. Lambiotte, and S. A. Orszag)	25
3.	Numerical Simulation of Turbulent Flow Over Wavy Walls (by R. Balasubramanian and S. A. Orszag)	41

INTRODUCTION

In this report, we summarize work done under NASA Contract NAS1-15844 on compressible shear flows and drag reduction. The report consists of this Introduction and the three following sections that summarize our progress on different aspects of this work.

In Section 1, we present a summary of some work on analytical and numerical aspects of conformal mapping. It describes a new and very efficient and robust method for computation of these maps in highly distorted geometries.

In Section 2, we describe the computer code SPECFD written for the CYBER-203 at NASA Langley Research Center. This code solves the three-dimensional time-dependent compressible Navier-Stokes equations by a mixed finite-difference-spectral algorithm. It works efficiently on the CYBER-203 with resolutions of 32 x 32 x 64 and promises to yield new insights into the nonlinear dynamics of compressible shear flows in wall-bounded geometries.

In Section 3, we describe our work on two-equation turbulence modelling of turbulent flow over wavy walls. A modified Jones-Launder model is used to include effects of the turbulence. This transport model has been implemented in a two-dimensional spectral code for flow in general wavy geometries. Results are presented for both flow over flat plates and flows over wavy walls.

1. Analysis of Numerical Conformal Mapping

Many two dimensional physical problems require the solution of Laplace's equation in a complicated domain Ω. One way to solve these problems is to conformally map Ω onto the unit disk $D(0,1)$ or a half plane $D(\infty)$. Once that is done the Poisson kernel provides the solution to the Dirichlet or restricted Neumann boundary value problems. Hilbert's generalization solves a mixture of the two where each applies on part of the boundary (but it doesn't solve the general Neumann boundary condition). Conversely any method of computing the Dirichlet or Neumann solution can be used to calculate the conformal map (see Theorem 5.3 of Dubiner 1981) but there is little reason to do it.

There exists a unique conformal mapping f of Ω onto $D(0,1)$ up to specifying $f(v)$ and $\operatorname{Arg} \partial_v f(v)$ for some $v \in \Omega$. Classical complex analysis demonstrates that on the boundary $\partial\Omega$, f is about as smooth as $\partial\Omega$ is and, of course, f is analytic inside. However, $[\partial_u f(u)]^{-1}$ is ill posed in terms of any reasonable norm of Ω even when u is restricted to be well away from $\partial\Omega$. For example take

$$\Omega = \frac{4}{\pi} \operatorname{arctanh}\left[\tanh \frac{\pi \ell}{4} \cdot D(0,1)\right] \tag{1}$$

where the notation means $\Omega = \{\frac{4}{\pi}\operatorname{arctanh}[\tanh\frac{\pi\ell}{4} z] \mid z \in D(0,1)\}$

It is a smooth domain which looks like an ellipse inflated inside a rectangle centered at the origin of length 2ℓ and width $2 - \frac{8}{\pi} \operatorname{arctanh}(e^{\frac{-\pi\ell}{2}})$. But the conformal mapping taking Ω to $D(0,1)$ and 0 to 0 is

$$f(u) = \coth \frac{\pi\ell}{4} \tanh \frac{\pi u}{4} \tag{2}$$

so

$$\frac{\partial_u f(u)|_{u=\ell}}{\partial_u f(u)|_{u=0}} = \cosh^{-2} \frac{\pi\ell}{4} \tag{3}$$

which decreases exponentially in ℓ and equals 0.000000603 for $\ell=10$! The curvature of $\partial\Omega$ near the ends relative to Ω's diameter is $0(\ell)$ but it is innocent of (3). The eccentric cigar shape of Ω is to blame and the same would happen for the smooth paddle-shaped domain of Figure 1.

Except near the ends example (1) is a slender domain. A domain Ω is called ε slender with ε small (say, $0<\varepsilon<\frac{1}{10}$) iff $\partial\Omega/\{\infty\}$ is composed of two connected components W_0 and W_1 such that for each $u \varepsilon W_0$

$$|\kappa(u,W_0)| \cdot |u-\tilde{u}| \leq \varepsilon \tag{4}$$

$$|\operatorname{Arg} \frac{dW_1|_{\tilde{u}}}{dW_0|_{u}}| \leq \varepsilon \tag{5}$$

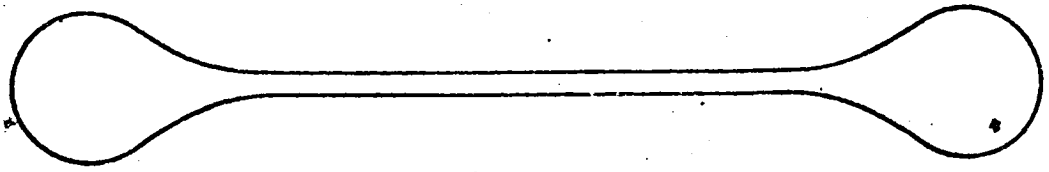

Figure 1

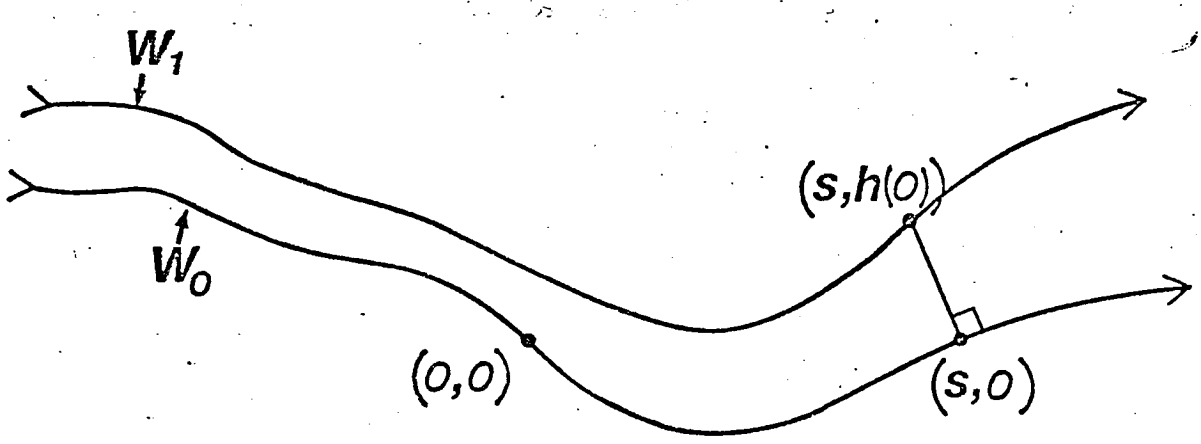

Figure 2

where $\tilde{u}=W_1$ minimizes $|\tilde{u}-u|$ and $\kappa(u,W_0)$ is W_0's curvature at u. Condition (4) requires W_0 to be nearly straight and condition (5) requires W_1 to be nearly parallel to W_0. Parametrize W_0 by its arc length s starting from an arbitrary fixed point. Each $u\in\Omega$ can be uniquely written as

$$u = W_0[s(u)] + t(u)\,\hat{n}[s(u)] \quad 0 < t < h[s(u)] \tag{6}$$

where $\hat{n}(s)$ is the inside unit normal at $W_0(s)$ and $h(s)$ is the distance of $\hat{n}(s)$ from $W_0(s)$ along the direction $\hat{n}(s)$ so that $W_0(s)+h(s)\hat{n}(s)\in W_1$. Let us normalize the coordinate system (s,t) in an approximately isotropic way

$$\tilde{g}(u) = \frac{\pi}{2}\left[\int_0^{s(u)} \frac{dp}{h(p)} + i\,\frac{t(u)}{h[s(u)]} - \frac{i}{2}\right] \tag{7}$$

The map $\tilde{g}$ from Ω onto $\Lambda=\{z\,|\,|\mathrm{Im}\ z|<\frac{\pi}{4}\}$ is quasi conformal with eccentricity bounded by $c\varepsilon$ (see Dubiner 1981 for definition). Let g be the exact conformal map from Ω onto Λ sending $W_0(\pm\infty)$ to $\pm\infty$ respectively. Clearly

$$f(u) = \tanh g(u) \tag{8}$$

conformally maps Ω onto $D(0,1)$ and so does

$$f(u,v) = \frac{f(u) - f(v)}{1-f(u)\overline{f(v)}}\, e^{ic(v)} \tag{9}$$

and it sends $v \in \Omega$ to 0. The real number c is determined by

$$\partial_1 f(v,v) > 0 \tag{10}$$

where ∂_1 denotes differentiation with respect to the first variable. Formula (8) is inserted in (9) and results in

$$f(u,v) = \frac{\sinh[g(u)-g(v)]}{\cosh[g(u)-g(v)]}\, e^{-i \operatorname{Arg}\partial_v g(v)} \tag{11}$$

and (11)'s derivative is

$$\partial_u f(u,v) = \frac{\partial_u g(u)}{\cosh^2[g(u)-\overline{g(v)}]} \cos[2\operatorname{Im} g(v)]\, e^{-i \operatorname{Arg}\partial_v g(v)} \tag{12}$$

Define $\tilde{f}(u,v)$ by replacing g with $\tilde{g}$ in (10). It is a quasi conformal map from Ω onto $D(0,1)$ of at most $c\varepsilon$ eccentricity sending v to 0. Hence $\tilde{f}(\cdot,v)$ is expected to be close to $f(\cdot,v)$ in some sense. Indeed (3.3) of Dubiner (1981) and others prove that

$$|\ln \partial_u \tilde{f}(u,v) - \ln \partial_u f(u,v)| \leq c\varepsilon\, |\tilde{g}(u)-\tilde{g}(v)| \tag{13}$$

where

$$\partial_u = \frac{1}{2}\,\partial_{\mathrm{Re}\,u} - \frac{1}{2}\,i\,\partial_{\mathrm{Im}\,u} \tag{14}$$

is defined on nonanalytic functions. Let us press on with the heuristics. Formula (12) for $\tilde{f},\tilde{g}$ shows that

$$\ell n\,|\partial_u \tilde{f}(u,v) = -\pi \left| \int_{s(v)}^{s(u)} \frac{dp}{h(p)} \right| - \ell n\ \ell n[s(u)] -$$

$$- \ell n\ \sin[\pi \frac{t(v)}{h[s(v)]} + 0(1) \tag{15}$$

$$\mathrm{Arg}\ \partial_u \tilde{f}(u,v) = -\alpha[0, W_0[s(u)], W_0] + 0(1) \tag{16}$$

where $\alpha[\cdot]$ is the change in angle of W_0 between $0=W_0[s(v)]$ and u's projection on W_0, $W_0[s(u)]$. Thus globaly f performs reasonable rotation but extreme scaling. In retrospect it should not be surprising because conformal maps are defined by being locally angle preserving with no scaling restrictions attached.

Formula (16) is easy to interpret. It obviously holds (up to translation in $\mathrm{Arg}\ \partial_u f(u)$ depending on its normalization) for $u \in \partial\Omega$, where Ω is a general domain. Thus (16) states that for slender domains

$$\left|\mathrm{Arg}\ \partial_1 f(\cdot,v)\right|_{u}^{\tilde{u}} = 0(1) \tag{17}$$

where the notation means $|\text{Arg}\, \partial_{\tilde{u}} f(\tilde{u},v) - \text{Arg}\partial_u f(u,v)\ | \leq c$ and $\tilde{u} \in \partial\Omega$ is near u, say the closest boundary point. The result (17) holds in general as proven by Theorem 5.4. of Dubiner (1981). Formula (15) is not that easy to generalize. Unlike (16), its right side depends on the structure of Ω between v and u. The first question is: what does 'between' mean in general? In order to gain some insight let us consider a more complicated example.

Let $0 < \varepsilon << 1$

$$\Omega(\varepsilon) = \{x+iy \ | \varepsilon x + \cos y > 0\} \tag{18}$$

The domain (18) has the following property. Any domain Ω is said to be a $\varepsilon > 0$ conjugation of the domains $\{\Lambda_\nu\}_{\nu \in I}$ iff for any $u \in \Omega$ there exists a $\nu \in I$ and two complex numbers a,b such that

$$u \varepsilon \Lambda(u) = a\Lambda_\nu + b \tag{19}$$

$$\sigma[u,\Lambda(u),\Omega] \leq \varepsilon \tag{20}$$

the distance from $\Lambda(u)$ to Ω relative to u is defined by

(10.113) in Dubiner (1981). The interested reader may prove

that any ε slender domain is a $c\varepsilon$ conjugation of

$$\Lambda_1 = \{x+iy \mid |y| < \frac{\pi}{4}\} \tag{21}$$

where $c>0$ is constant. Domain (18) is a $c\varepsilon$ conjugation of Λ_1 and

$$\Lambda_2 = \{x+iy \mid x - \frac{1}{2}y^2 > 0\} \tag{22}$$

$$\Lambda_3 = \hat{c}\backslash(-\Lambda_2) = \{x+iy \mid x + \frac{1}{2}y^2 > 0\} \tag{23}$$

$$\Lambda_4 = \hat{c}\backslash\bigcup_{n=-\infty}^{\infty} [-\infty, i(2n+1)\pi] \tag{24}$$

where $[a,b]$ is the closed interval between a and b. We have to match the conformal maps from all the $\Lambda(u), u\varepsilon\Omega(\varepsilon)$. In this case it is easiest to do when considering $f[\cdot,\infty,\Omega(\varepsilon)]$, the conformal map from $\Omega(\varepsilon)$ onto the half plane $D(\infty)$ normalized by

$$\partial_1 f(+\infty,\infty) = 1 \tag{25}$$

The domain $\Omega(\varepsilon)$ is periodic and symmetric so we can limit ourselves to

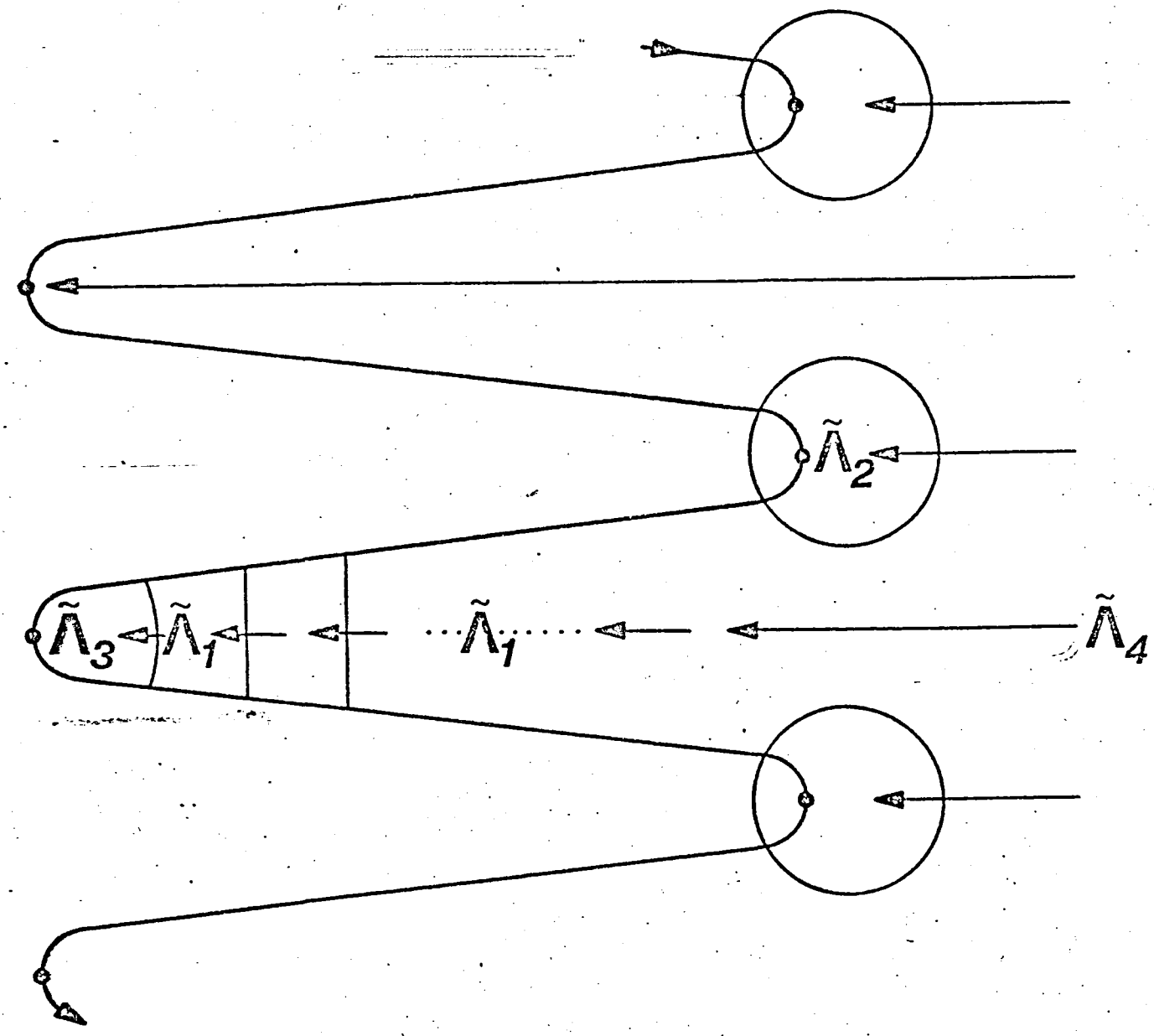
$\tilde{\Lambda}_2$
$\tilde{\Lambda}_3$
$\tilde{\Lambda}_1$
$\tilde{\Lambda}_1$
$\tilde{\Lambda}_4$

Figure 3

$$u = x + iy \qquad 0 \leq y \leq \pi \tag{26}$$

We start from

$$f(u, \infty, \Lambda_4) = 2 \operatorname{arcsinh} e^{\frac{1}{2}u} \tag{27}$$

It is modified to

$$x > \frac{1}{\varepsilon} - 0\ (\frac{1}{\sqrt{\varepsilon}}) \qquad |x - \frac{1}{\varepsilon} + i(y-\pi)| >> \varepsilon \tag{28}$$

$$\tilde{f}[x + iy, \infty, \Omega(\varepsilon)] = 2 \operatorname{arcsinh} e^{\frac{1}{2}(x - \frac{1}{\varepsilon}) + iy \frac{\pi}{2h(x)}} \tag{29}$$

where

$$h(x) = \begin{cases} \arccos(-\varepsilon x) & -\frac{1}{\varepsilon} \leq x \leq \frac{1}{\varepsilon} \quad (30) \\ \pi & \frac{1}{\varepsilon} < x \quad (31) \end{cases}$$

and the exact limitation (28) will follow from comparison with the following formulas. A priori rigorous bounds can be derived but as usual it is inconvenient. Next

$$f(u, \infty, \Lambda_1) = i\, c\, e^{2u} \tag{32}$$

(there is no natural normalization). We already know how to match the $f[u,\infty,\Lambda(u)]$'s where $\Lambda(u)=a\Lambda_1+b$: recall (7,8). They match with (28,29) and give

$$-\frac{1}{\varepsilon} < x < \frac{1}{\varepsilon} + 0\left(\frac{1}{\sqrt{\varepsilon}}\right) \;,\quad |x + \frac{1}{\varepsilon} + iy| >> \varepsilon,\ |x - \frac{1}{\varepsilon} + i(y-\pi)| >> \varepsilon \tag{33}$$

$$\tilde{f}[x+iy,\infty,\Omega(\varepsilon)] = 2e^{\frac{\pi}{2}\left[\frac{si[h(x)]-si(\pi)}{\varepsilon} + i\,\frac{y}{h(x)}\right]} \tag{34}$$

where

$$si(p) = \int_0^p \frac{\sin q}{q}\, dq \tag{35}$$

Now we can match $f(\cdot,\infty,\Lambda_2)$ to (33,34). and obtain

$$|x + \frac{1}{\varepsilon} + iy| << \varepsilon^{-1/3} \tag{36}$$

$$\tilde{f}[x+iy,\infty,\Omega(\varepsilon)] = 4e^{-\frac{\pi si(\pi)}{2\varepsilon}} \cos\left[\frac{\pi}{2}\sqrt{1 - \frac{2}{\varepsilon}[x + \frac{1}{\varepsilon} + iy\,\frac{\sqrt{2\varepsilon x+2}}{h(x)}]}\right] \tag{37}$$

Similarly, $f(\cdot,\infty,\Lambda_3)$ is matched to (28,29):

$$|x + \frac{1}{\varepsilon} + i(y-\pi)| << 1 \tag{38}$$

$$\tilde{f}[x+iy,\infty,\Omega(\varepsilon)] = \sqrt{2\varepsilon}\left(\sqrt{1+\frac{2}{\varepsilon}[x-\frac{1}{\varepsilon}+i[y-h(x)]}-1\right) \tag{39}$$

In particular the maximum and minimum of $|\partial_u f[u,\infty,\Omega(\varepsilon)]|$ are obtained at $\frac{1}{\varepsilon}+i\pi$, $-\frac{1}{\varepsilon}$ respectively and

$$\partial_1 f[\frac{1}{\varepsilon}+i\pi,\infty,\Omega(\varepsilon)] \sim \sqrt{\frac{2}{\varepsilon}} \tag{40}$$

$$\partial_1 f[-\frac{1}{\varepsilon},\infty,\Omega(\varepsilon)] \sim \frac{2\pi}{\varepsilon}\, e^{-\frac{\pi si(\pi)}{2\varepsilon}} \tag{41}$$

What have we learned from example (18)? Figure 3 illustrates the direction of information flow (The reverse of the direction of dependence) which were exhibited while $f[\cdot,\infty,\Omega(\varepsilon)]$ has been constructed. The situation is quite special yet we have some grounds to suspect that in general $\partial_u f(u,v,\Omega)$ and other functions depend mainly on Ω's part 'around' the curve of least Euclidean distance between v and u <u>inside</u> Ω. A close inspection of (27-38) reveals that the above mentioned curve from to u resembles

$$\Gamma(\infty,u,\Omega) = \{w\varepsilon\Omega \mid 0 < \frac{f(w,\infty,\Omega)}{f(u,\infty,\Omega)} < 1\} \tag{42}$$

The curvces $\Gamma(u,v,\Omega)$ are called geodesics because they are the geodesics of a certain conformally invarient metric

$p(u,v,\Omega)$ of Theorem 1.1. Some geodesics of Λ_1 are illustrated in Figure 0.4. Notice for any two $u,v\epsilon\Lambda_1$ far away the most of (u,v,Λ_1) is exponentially close to Λ_1's axis of symmetry. Theorem 8.3 demonstrates that in general the geodesics try to keep away from the boundary.

The connection between geodesics and lines of least Euclidian distance is proven in Theorem 9.2 (Dubiner 1981).

Now that we have some idea on what 'between' and means it is time to find out how the rest of Ω affects $\ell n\ \partial_u f(u,v,\Omega)$ and other quantities. For that purpose let us return to ε slender domains and compute a next order correction to (7). We start by calculating $\partial_u \tilde{g}$. The gradient of (6) is

$$du = \hat{n}[s(u)][(-i+t(u)\partial_s \ell n\ \hat{n}[s(u)])ds + dt] \tag{43}$$

and of (7)

$$d\tilde{g}(u) = \frac{\pi}{2h(s)}[(1-it(u)\partial_s \ell n\ h(s))ds + idt] \tag{44}$$

Formulas (43,44) combine into

$$d\tilde{g} = \frac{\pi}{4h\hat{n}} \left[2i + \frac{t\partial_s \ell n(h\hat{n})^{\cdot}}{1+it\partial_s \ell n\hat{n}}\right] du -$$

$$- \frac{n}{4h} \frac{t\partial_s \ell n(hn)}{1+it\partial_s \ell nn} du \qquad (45)$$

Define the $\tilde{g}$ correction function

$$g_1 = g - \tilde{g} \qquad (46)$$

Then

$$\partial_{\underline{u}} g_1 = - \partial_{\underline{u}} \tilde{g} = - 2\pi i \frac{\hat{n}}{h} \mu = - 2\pi i \eta \qquad (47)$$

$$\text{Im } g_1 | \partial\Omega = 0 \qquad (48)$$

where

$$\mu(u) = \frac{1}{8} \frac{it(u)\partial_s \ell n(h[s(u)]\hat{n}[s(u)])}{1+it(u)\partial_s \ell n\hat{n}[s(u)]} \qquad (49)$$

Notice that Ω is $0(\varepsilon)$ slender iff

$$\sup_{u\varepsilon\Omega} |\mu(u)| \leq c\varepsilon \qquad (50)$$

Problem (47,48) has a unique solution up to an additive real constant

---

(51)

$$g_1(u) = -i \int_\Omega \int \left[\frac{\eta(w)\partial_w f(w)}{f(u)-f(w)} - \frac{\overline{\eta(w)\partial_w f(w)}}{\frac{1}{f(u)} - \overline{f(w)}} \right] |d^2w|$$

$$g(u) = \tilde{g}(u) = i \int_\Omega \int \left[\eta(w)\partial_w g(w) \coth[g(u)-g(w)] - \right.$$

$$\left. - \frac{}{\overline{\eta(w)\partial_w g(w)}} \tanh[g(u)-\overline{g(w)}] \right] |d^2w| \qquad (52)$$

where

$$|d^2w| = d\,\mathrm{Re}\,w \cdot d\,\mathrm{Im}\,w \qquad (53)$$

Formula (51) is an integral equation of the first kind which can be iterated to convergence. The first order correction to $\tilde{g}$ with some modifications is

$$g(u) \sim U + \int_\Omega \int [\mu(w)\coth(U-W) + \overline{\mu(w)}\tanh(U-W)]\,|d^2w| \qquad (54)$$

where we have and will abbreviate

$$U = \tilde{g}(u), \quad V = \tilde{g}(v), \quad W = \tilde{g}(w) \qquad (55)$$

Recall (11)

$$\ell n\ f(u,v) = \ell n\ \frac{\sinh(U-V)}{\cosh(U-\bar{V})} - \frac{1}{2}\ \ell n\ \frac{\partial_v V}{\partial_v \bar{V}} \tag{56}$$

so

$$\ell n\ f(u,v) \sim \ell n\ \tilde{f}(u,v) +$$

$$+ \int\int_{\Omega} [\mu(w)K(U,V,W) + \overline{\mu(w)}K(U,V,\bar{W}+i\tfrac{\pi}{2})]\ |d^2w| \tag{57}$$

$$K(U,V,W) = \coth(U-V)[\coth(U-W) - \coth(V-W)] -$$

$$- \tanh(U-\bar{V})[\coth(U-W) - \tan\imath(\bar{V}-W)] +$$

$$+ \frac{1}{2}\sinh^{-2}(V-W) - \frac{1}{2}\sinh^{-2}(\bar{V}-W) =$$

$$= \frac{\cos(2\mathrm{Im}\ v)}{2\sinh(U-W)\sinh(V-W)\sinh(\bar{V}-W)}\left[\frac{\sinh(U-V)}{\sinh(U-W)} - \frac{\cosh(U-\bar{V})}{\cosh(\bar{V}-W)}\right] \tag{58}$$

and

$$\ell n\ \partial_u f(u,v) = \ell n\ f(u,v) + \ell n\ \partial_u\ \ell n\ f(u,v) \tag{59}$$

so

$$\ln \partial_u f(u,v) = \ln \partial_u \tilde{f}(u,v) +$$

$$+ \iint_{\Omega} [\mu(w)L(U,V,W) + \overline{\mu(w)}L(U,V,\overline{W}+i\,\tfrac{\pi}{2}]\ |d^2w| \qquad (60)$$

$$L(U,V,W) = K(U,V,W) + \frac{\partial_u K(U,V,W)}{\partial_u \tilde{f}(u,v)} =$$

$$= \frac{1}{2\sinh(U-W)\sinh(V-W)\sinh(\overline{V}-W)} \left[\frac{\cos(2\mathrm{Im}v)\sinh(U-V)}{\sinh(V-W)} - \right.$$

$$\left. - \frac{\cos(2\mathrm{Im}v)\cosh(U-\overline{V})}{\cosh(\overline{V}-W)} + 2\,\frac{\sinh(U-v)\sinh(U-\overline{V})}{\sinh(V-W)}\right]$$

(61)

If we assume that $\mu(w)$ is not only of order ε but is also slowly varying, for instance $\frac{1}{h(s)}\ |\partial_s \mu[W_0(s)+h(s)\hat{n}(s)]| \leq c\varepsilon^2$ then the integration in (57,60) can be done explicitly. Of course that results is much easier to derive directly and is of no interest to us. What we have wanted and obtained is the relative dependence of $\partial_u f(u,v)$ on the boundary part $\alpha = W_0([s-\frac{1}{2}\Delta s, s+\frac{1}{2}\Delta s])$ centered at $w = W_0(s)$ of length Δs. When

$$0 < \Delta s \leq h(s) \leq |u-w|\ ,\ |v-w| \qquad (62)$$

the contrlling factor of α's influence is

$$e^{-4\inf|\tilde{g}(w) - [\tilde{g}(v),\tilde{g}(u)]|} \sup|\mu(\alpha)|\ \frac{\Delta s}{h(s)} \qquad (63)$$

The asymptotically correct term is the same with $\tilde{g}$ replaced by g. A graphic interpretation of (63) follows. In order to affect $\partial_u f(u,v)$ the data about α's shpae must travel from α to v. It is provided a free ride in Ω's portion between u and v (in general on the geodesic $\Gamma(u,v)$ between u and v) but it must pay $\frac{\pi}{2h[s(z)]}$ per distance for travel around any point z not between u and v. The data is thrifty so it will move along a geodesic (a cost minimizing curve which turns out to agree with (42) to some point 0 between v and u and will then enjoy a free ride to v. The optimal choice of 0 is the middle point among u,v,w. Let us call the total minimal cost $\rho_x(w,\Delta s,u,v)$. Then when the α data reaches v its intensity is deminished by a factor of $e^{-4\rho_x}$. A similar situation holds for other function of the conformal map besides $\ell n \partial_u f(u,v)$, except that the ride on the geodesic between u and v is not free but on a reduced fare. For instance (57,58) shows that the controlling factor of α's influence on $\ell n\, f(u,v)$ is

$$e^{-2\inf|\tilde{g}(w)-[\tilde{g}(v),\tilde{g}(u)]|-2|\tilde{g}(w)-\tilde{g}(v)|}\sup|\mu(\alpha)|\frac{\Delta s}{h(s)} \qquad (64)$$

which means that the travel on $\Gamma(u,v)$ is done on a half fare. Notice that this does not change 0, the point of transfer to $\Gamma(u,v)$.

Now that we know what (63) means let us understand

where it comes from. The term $e^{-2\rho_x}$ is simply the decay of a Dirichlet or Neumann data from α to $\Gamma(u,v)$ and is already present in (54). However, in the computation of (58) a cancellation has occurred and another $e^{-2\rho_x}$ has appeared. Lest it look like a freak accident let us derive it from another point of view, close in spirit if not in technical complexity to section 10's. Suppose that Ω is not only ε slender but is ε close to Λ. If w is between u and v than $\rho_x = 0$ so let us consider v between u and w (the remaining case is similar). Define

$$\hat{f}(z) = \tanh(z - \mathrm{Re}\ v) \tag{65}$$

The domain $\hat{f}(\Omega)$ is close to the unit disk. The image of α has length of order $e^{-2\rho_x}\Delta s$. A major change in α modifies $\hat{f}(\Omega)$ by a region away from $\hat{f}(u)$, $\hat{f}(v)$ whose area is of order $(e^{-2\rho_x}\Delta s)^2$. The details will be presented in Section 10 but it takes no great leap of imagination to conclude that α's effect is at most proportional to that area, and that is where the extra $e^{-2\rho_x}$ comes from. What about $g(u)$? It is normalized so that $g(\pm\infty) = 1$ and $|\hat{f}(w) - 1|$ or $|\hat{f}(w) + 1|$ is of order $e^{-2\rho_x}$ so α's influences on $g(u)$ is of order $\frac{(e^{-2\rho_x}\Delta s)^2}{e^{-2\rho_x}}$.

The interpretation of (63,64) was chosen so that it is generalizable to arbitrary domains, with some modifications.

The asymptotic theory has to be replaced by estimation up to a constant factor. The measure μ of Ω's deviation from Λ's shape is special and anyway there is no ideal general domain. Instead we will pick a wide challange and consider a perturbation of a general domain Ω to a specified general domain $\tilde{\Omega}$. We will divide the perturbation into parts and as in Theorem 10.5 I show that each such part α of diameter Δs centered at w affects $\ell n\, \partial_u f(u,v)$ by $\delta_x^2(w,\Delta s,u,v)$ which is a generalization of (63) with $\sup|\mu(\alpha)|$ replaced by $\frac{\Delta s}{h(s)}$. The term $\delta(w,\Delta s,u,v)$ is first encountered in Theorem 8.6 and

$$\delta_x(w,\Delta s,u,v) = \sup_{0\in\Gamma(u,v)} \delta(w;\Delta s,u,v) \qquad (66)$$

The general interaction between u,v,w and 0 is described by Theorem 4.6, which should be combined with Theorem 9.2 (Dubiner 1981).

The local length scale $h[s(w)]$ is generalized into $a(w,u,v)$ of (9.2). Its dependence on u,v is unfortunatly unavoidable: consider a half plane Ω $D(\infty)$. The lack of a local length scale, except of $\inf|w-\partial\Omega|$ which vanishes on the boundary is the most important general ingredient missing in slender domains. It is not fortuitous that the conformal metric $\rho(u,v)$ blows up at the boundary.

Our examples were mostly of smooth domains but notice that domain (18) has a very sharp bend at $\frac{1}{\varepsilon}+i\pi$, which

corresponds to Λ's corner, and it did not distrub us from completing a uniform asymptotic approximation. Theorem (10.7) proves an interesting property of a fractal, which is the applied mathematician's ultimate in roughness. However, we insist on obtaining specific estimates at specific points, in contrast to the 'average' type approach of P.D.E. Theory. That is an advantage when it works but it fails near a rough boundary. In Sec. 5 of Dubiner (1981) it is shown how to patch our results with P.D.E. Theory. Some synthesis is clearly required.

Let us now consider the numerical computation of conformal mappings. As remarked earlier, any Laplace solver will do. Suppose that the domain Ω is covered by $0(N^2)$ points, N of which are on the boundary $\partial\Omega$. Then a Laplace solver requires storing $0(N^2)$ numbers and performing from $0(N^2 \ell n\ N)$ to $0(N^3)$ operations, where the last estimate is more realistic for complicated domains. The grid set up is is troublesome, especialy for multiscaled and time dependent (free boundary) domains.

One way to avoide an internal grid is using a vortex representation. That results in an integral equation of the first kind which is numerically formulated as a set of $N \times N$ linear equations. It can be solved by by Gaussian elimination which requires $0(N^2)$ memory locations and $0(N^3)$ operatios. Alternativly one may iterate the system using $0(N)$ memory and

$O(N^2)$ operations per iteration. This is the numerical approximation to Neumann's series, and the later is guaranteed to converge for any single sheeted domain satisfying some mild conditions. The best existing Rayleigh-Taylor instability simulation has been done in that way by Baker, Meiron and Orszag (1981). It is relatively easy to program and generalize to 3 dimensions. Moreover it can handle two incompressible fluids problems which conformal mapping alone can not solve unless the fluids density ratio is 0 or 1. However, Neumann's series's convergence is precarious. The arte of convergence for the domain Ω equals that for its exterior domain c Ω^c and in particular convergence fails for multi-sheeted domains and is very slow when two separate parts of $\partial\Omega$ approach each other. The domain (18) requires $O(\frac{1}{\varepsilon})$ iterations per order reduction in the error. Moreover the Neumann series seems hard to modify in a way which will extract a singularity such as a corner and still preserv convergence for general domains.

The most natural numerical conformal mapping computation is done by Taylorexpanding the conformal function from the unit disk onto Ω. Several such methods are listed in Sec. I. The best of them takes only $O(N)$ memory locations and $O(N^2 \ell n\ N)$ operations but we have seen that the series will not converge to domain (18) before $N = e^{c/\varepsilon}$ terms are taken

The first direct computation of the conformal map onto a

cigar shaped domain has been done by Menikoff and Zemach (1980). Their method is to set up a system of $N \times N$ nonlinear equations and solve then by Newton iteration. Each iteration takes $0(N^2)$ memory and $0(N^3)$ operations and only few iterations are required.

Any partial differential equation on a time dependent domain can be solved by a Green's function method which utilizes only boundary data. This is not usually done because it takes $0(N^{2d-2})$ memory locations and $0(N^{2d-2})$ operations in d dimensions which is unreasonable for $d \geq 3$. For the ∇^2 operator in 2 dimensions better can be done because then the Green's function $G(u,v,\Omega)$ is constructable from from $G(u,v_0,\Omega)$ and its harmonic conjugate where v_0 is constant. That is the basis of our method, though it will be presented in a different way. It takes $0(N)$ memory locations and $0(N^2)$ operations.

REFERENCES

M. Dubiner 1981 Theoretical and Numerical Analysis of Conformal Mapping, Ph. D. Thesis, Department of Mathematics, M.I.T., Cambridge, MA.

R. Menikoff & C. Zemach 1980 Methods for Numerical Conformal Mapping, J. Comp. Phys. 36, 366.

2. NUMERICAL SIMULATION OF COMPRESSIBLE SHEAR FLOWS ON THE CYBER-203

INTRODUCTION

The objective of this work is the development of an algorithm for the numerical simulation of three-dimensional viscous compressible flows. This code is applied to basic studies of compressible shear flows at high Reynolds number, such as the simulation of the incipient stages of transition to turbulence, and receptivity of laminar boundary layers to external disturbances. Since the physical instabilities involved in such problems are of a delicate nature which could be easily masked by numerical instabilities or other errors, it is essential to use an accurate numerical algorithm that can be efficiently implemented on the Control Data Corp. CYBER-203.

The primary purpose of this paper is to describe the mixed spectral-finite difference code, SPECFD, as coded for the CYBER-203. We will focus on the vectorization techniques for some of the computational procedures with careful attention to the interplay between the storage allocation, the vectorization techniques, and their combined effects on input/output (I/O) requirements for this virtual memory machine.

The next section describes the numerical method. We then discuss the characteristics of the CYBER-203 at NASA Langley Research Center. The next section describes vectorization techniques including data base design and computational procedures. Finally, the overall flow of the code is outlined and a timing analysis of the various parts is presented.

Governing Equations and Solution Technique

The compressible Navier-Stokes equations are

$$\frac{\partial \vec{q}}{\partial t} = - \left[\vec{q} \cdot \nabla \vec{q} + \frac{1}{\rho} \nabla p - \left(\frac{1}{\rho} \right)_{av} \nabla p \right] - \left\{ \left(\frac{1}{\rho} \right)_{av} \nabla p \right\} + \nabla \cdot \bar{\bar{\tau}}$$

$$\frac{\partial \rho}{\partial t} = - q \cdot \nabla \rho - \rho \nabla \cdot \vec{q}$$

$$\frac{\partial p}{\partial t} = - \left[\vec{q} \cdot \nabla p + r(\rho - \rho_{av}) \nabla \cdot \vec{q} \right] - \left\{ \gamma p_{av} \nabla \cdot \vec{q} \right\} + \frac{\gamma}{Pr} \nabla \cdot \mu \nabla \left(\frac{p}{\rho} \right) + (\gamma - 1) \Phi ,$$

where $q, \rho, p, \bar{\bar{x}}, \Phi, \alpha, Pr$ is the velocity vector, density, pressure, viscous stress tensor, viscous dissipation, ratio of specific heats, and Prandlt number, respectively. The constitutive relation for the stress tensor is

$$\bar{\bar{\tau}} = \lambda \nabla \cdot \vec{q} \, \bar{\bar{I}} + \mu (\nabla \vec{q} + \nabla \vec{q}^{T})$$

where λ is assumed equal to $-\frac{2}{3}\mu$ and μ is given by Sutherland's formula

$$\mu = 1.4582 \times 10^{-6} \, T^{3/2} / (T + 110.33) \; p_a\text{-sec}$$

The expression for viscous dissipation is

$$\Phi = \lambda (\nabla \cdot \vec{q})^2 + \frac{\mu}{2} [(\nabla \vec{q}) + (\nabla \vec{q})^T] * [(\nabla \vec{q}) + (\nabla \vec{q})^T].$$

The assumption of a calorically perfect gas is implicit in this formulation.

The addition and subtraction of the term $(1/\rho)_{av} \nabla p$ in the momentum equation and a similar manipulation in the equation for pressure require explanation. $(1/\rho)_{av}$ is the average of the specific volume on each horizontal x-y plane and hence is a function of the z-coordinate only. The Crank-Nicolson method is used on the pressure term in the curly bracket. We resort to this kind of artifact to ensure convective stability at low Mach numbers without having the severe time step restriction demanded by an explicit method.

Boundary Conditions

We choose periodic boundary conditions in the streamwise (x) and spanwise (y) directions. This permits spectral representation of the dependent variables in these two directions. In the normal (z) direction we use no-slip boundary condition on the

plate ($z = 0$). Using $\zeta = az/(az+b)$, the semi-infinite physical domain $0 \leq z < \infty$ is mapped onto the computational domain $0 \leq \zeta \leq 1$. Zero perturbation boundary conditions are applied at $\zeta = 1$. For free shear flows, the physical domain $-\infty < z < \infty$ is mapped onto $0 \leq \zeta \leq 1$ using a hyperbolic tangent transformation. Zero perturbation boundary conditions are applied at both top and bottom boundaries.

Numerical Method

The numerical method consists of three stages (fractional steps) based on the well-known technique of operator splitting [1]. The first fractional step includes the effect of the advection terms:

$$\vec{q}^{\,*} = \vec{q}^{\,n} + (\Delta t_1 + \Delta t^n)\left[-\vec{q}^{\,n}\cdot\Delta\vec{q}^{\,n} - \left\{\frac{1}{\rho^n} - \left(\frac{1}{\rho^n}\right)_{av}\right\}\nabla\,\rho^n\right]$$

$$- \Delta t_1\left[-\vec{q}^{\,n-1}\cdot\nabla\vec{q}^{\,n-1} - \left\{\frac{1}{\rho^{n-1}} - \left(\frac{1}{\rho^{n-1}}\right)_{av}\right\}\nabla\,\rho^{n-1}\right]$$

$$- \frac{1}{2}\Delta t^n \left(\frac{1}{\rho^n}\right)_{av} \nabla\,\rho^n \qquad (1)$$

$$\overset{*}{\rho} = \rho^n + (\Delta t_1 + \Delta t^n)\,[-\vec{q}^n \cdot \Delta\rho^n - \rho^n \nabla \cdot \vec{q}^n]$$

$$- \Delta t_1 [-\vec{q}^{n-1} \cdot \nabla \rho^{n-1} - \rho^{n-1} \nabla \cdot \vec{q}^{n-1}]$$

$$\rho^* = \rho^n + (\Delta t_1 + \Delta t^n)[-\vec{q}^n \cdot \nabla \rho^n - r(\rho^n - \rho^n_{av}) \nabla \cdot \vec{q}^n]$$

$$- \Delta t_1 [-\vec{q}^{n-1} \cdot \nabla \rho^{n-1} - r\,(\rho^{n-1} - \rho^{n-1}_{av}) \nabla \cdot \vec{q}^{n-1}]$$

$$- \tfrac{1}{2} \Delta t^n \rho_{av} \nabla \cdot \vec{q}^{\,n}$$

where $\Delta t_1 = (\Delta t^n)^2 / (2\Delta t^{n-1})$. A variable-step second-order Adams-Bashforth method has been used for time discretization. The pseudospectral method is used for calculating x- and y-derivatives, and central differences are used to evaluate z-derivatives (using an equally spaced grid in the ζ variable).

The second fractional step is an implicit pressure correction:

$$q^{**} + \tfrac{1}{2} \Delta t^n \left(\frac{1}{\rho^n} \right)_{av} \nabla \rho^{**} = \vec{q}^*$$

$$\rho^{**} + \tfrac{1}{2} \Delta t^n \; r \, \rho^n_{av} \nabla \cdot \vec{q}^{**} = \rho^*$$

This system of equations is reduced to a single Helmholtz equation for p^{**}:

$$p^{**} - \frac{1}{4}\Delta t^{n^2}\, r\ \rho_{av}\nabla\cdot\left[\left(\frac{1}{p^n}\right)_{av}\nabla p^{**}\right] = \rho^* - \frac{1}{2}\Delta t^n\ r\ \rho_{av}\nabla\cdot\vec{q}^* = Q^* \tag{3}$$

Using a spectral representation for p^{**} in the x- and y-directions and central finite difference in the z-direction there results a tridiagonal matrix equation for p^{**} in wave number space.

In the third fractional step, viscous corrections are added to the inviscid solution obtained in the previous two steps. Use of the pseudospectral technique for the evaluation of viscous terms entails a rather unreasonable increase in the number of FFT's per time step [2]. Consequently, the viscous terms are discretized using central differences. The truncation error is on the order of $\nu(\Delta t + \Delta\mu^2 + \Delta y^2 + \Delta z^2)$ where ν is the maximum kinematic viscosity. This error is small since ν is small in the high Reynolds number flows of interest. Further, the well-known problem of artificial viscosity (due to the truncation

error of the advection terms) swamping the physical viscosity does not arise in the present algorithm, as the advection terms are evaluated pseudospectrally. To avoid severe time step restrictions resulting from small Δz in the stretched z-mesh, the z-derivatives are treated implicitly. This results in tridiagonal matrices for u,v,w, and p.

We write this three level time split scheme symbolically as

$$U^{n+1} = \mathcal{L}_V \, \mathcal{L}_I \, \mathcal{L}_E \, (U^n , U^{n-1})$$

where $U = (u,v,w, ,p)^T$ and T indicates transpose. Here the subscript E indicates the explicit step, I the implicit pressure step, and V the viscous step.

Characteristics of the CYBER-203

The CYBER-203 is a vector processing computer manufactured by the Control Data Corporation (CDC). As a vector processor, it can perform vector operations on 64-bit (32 bit) data at a peak rate of 50 (100) MFLOPS (millions of floating operations per second) 25 (100) MFLOPS for multiplication, and 12.5 (50) MFLOPS for division. With each vector operation there is a vector startup which is independent of the vector length. Vector operations of length 1000 achieve 80 to 85% of their peak rate. This is about four times faster than vectors of length 75. Consequently, it is desirable to use long vectors where possible. The ability to do this depends upon the algorithm being used as well as the storage scheme selected by the program designer. The CYBER-203 can also do scalar processing and in this mode generally will execute two to three times faster than the CDC CYBER-175. The CYBER-203 has a virtual memory implemented as "small" pages (512 words) or "large" pages (65,536 words). The CYBER-203 at Langley Research Center has 1025K, 64-bit words of semiconductor memory (16 large pages). One can effectively double the memory capacity by using the 32-bit word length features.

Vectorization Techniques

The data base design and vectorization techniques are inter-related on the CYBER-203 since vectors, by definition, are contiguous locations in memory.

Notation:

We first introduce some notation helpful in describing these two facets of the implementation. Assume that the dimensions of the grid in the x,y,z directions are I,J,K. U will refer to the vector $(u,v,w,p,\rho)^T$ and an operator such as $\frac{\partial}{\partial x}$ operating on U should be applied to each component of U. References to a "plane" of data are to one of the x-y planes. These are typically the vectors used in our code. U(k) refers to the kth plane. The Thomas algorithm for solving a tridiagonal system requires the storage of two pieces of data for each equation, and consequently each grid point: $(\alpha_w(k),\beta_w(k))$ are the kth plane of such data for the w-momentum equation. Also, U^* is the result of the $\mathcal{L}_E$ operator on U^n, U^{**} the result of the $\mathcal{L}_I$ operator, and U^{n+1} the result of the $\mathcal{L}_V$ operator.

Data Base Design:

We wish to accomplish two things with our data base design: (1) a storage scheme that permits operation on long vectors, preferably over an entire plane of the three dimensional grid, and (2) a scheme that allows controlled paging by the virtual system. With this in mind, each variable which is required over the entire grid is stored on one x-y plane at a time, with all variables at the kth plane stored in succession (see Fig. 1). The execution flow is then to do all computations possible at plane k before proceeding to plane k+1. It has been shown [3] that this data layout and computational strategy is important for controlling paging when the large pages are involved. The paging per time step is further reduced by (1) marching forward, then in reverse through the data base (z-direction) and (2) applying all three operators in one forward-reverse sweep. The first technique permits the I/O requirements for each time step to be proportional to the amount by which the data base exceeds central memory [3] and the second technique means that only one pass through the data base is required per time step instead of three. The latter approach does cause some

programming inconvenience when computing the z-derivatives. For instance, the $\mathcal{L}_I$ operator computation at the kth plane requires $u^*(k+1) - u^*(k-1)$, where u^* is computed by the $\mathcal{L}_E$ operator. The requirement for $u^*(k+1)$ implies that the L_I operator must be lagged one plane behind the $\mathcal{L}_E$ operator.

Main Computation Modules:

There are three algorithms which are a major part of the overall computational procedure and which have been vectorized for the CYBER-203. These are:

1. One Dimensional Fast Fourier Transform (1-D FFT)

The x and y derivatives in the $\mathcal{L}_I$ and $\mathcal{L}_E$ operators are computed using the one-dimensional FFT. For instance

$$\frac{d}{dx} u(x) = F^{-1} (i\omega g(\omega)),$$

where $g(\omega)$ is $F(u)$, the Fourier transform of u with respect to the x variable and ω is the wave number. The CYBER-203 implementation described in reference [4] is used and will be detailed more fully under the section "Performance".

2. Two-Dimensional Fast Fourier Transform (2-D FFT)

The $\mathcal{L}_I$ operator involves applying the two-dimensional FFT operator, F_{xy}, to equation (3). If we define

$$\tilde{P}^{**}(k_x,k_y,z) = F_{xy}P^{**}(x,y,z),$$

then the resulting second order differential equation in z for P^{**} can be central differenced leaving an independent tridiagonal system, implicit in the z-direction, for each (k_x,k_y) wave number. The right-hand side for each system is the appropriate element from $F_{xy}Q^*$. The coefficients can be analytically determined. The solution to each system yields $P^{**}(k_x,k_y,z)$ and then one computes

$$P^{**}(x,y,z) = F_{xy}^{-1}\tilde{P}(k_x,k_y,z).$$

The CYBER-203 software described in reference (5) is used to apply F_{xy} and F_{xy}^{-1}.

3. Systems of Tridaigonal Equations

The $\mathcal{L}_I$ and $\mathcal{L}_V$ operators both generate systems of tridiagonal equations implicit in the z-direction

There is an independent system for each (k_x,k_y) or (x,y) point, respectively, in a plane. The usual Gauss elimination based tridiagonal solver, frequently called the Thomas algorithm, is inherently scalar but since we must solve, say , $M = I \times J$ systems simultaneously, vectors of length M can be used. The forward sweep of the Thomas algorithm is done a plane at a time saving only the pairs $(\alpha(k), \beta(k))$ required for the back substitution of a unit upper bidiagonal system of equations. Since the variables are interleaved a plane at a time, the storage is appropriate for both the long vectors and the controlled paging.

Performance

The CPU efficiency of any highly vectorized program on a vector computer like the CYBER 203 relative a particular scalar computer is directly proportional to the vector lengths involved. This is true assuming:

1. The same algorithms are implemented in both the scalar and vector computers.

2. No extra work, typically in form of data movement, is required to achieve the vector lengths used.

Program SPECFD is highly vectorized. For an I x J x K grid all vector operations, except the evaluation of the one and two dimensional FFTs are of length I*J or I*J+2I and, hence, quite efficient. The derivative evaluation by the FFT routine is somewhat more difficult to analyze.

The software to implement the FFT algorithm simultaneously computes the one-dimensional FFT of M independent complex data sets each of size N. It requires that the first components of each data set to be stored consecutively, followed by the second components, etc. With this arrangement, it achieves average vector lengths of Mlog N. It is obvious that the data structure is quite important and that increases in M will yield higher CPU efficiency.

The total data base includes 17 variables stored over the entire grid. These are (u,v,w,p,ρ), their respective convective derivatives $(du,dv,dw,dp,d\rho)$ from the previous timestep for the explicit operator, and the four Thomas algorithm pairs (α_u,β_u), (α_v,β_v), (α_w,β_w), and (α_p,β_p). Since $\alpha_u = \alpha_v$ only one of these is stored. For a 32 x 32 x 64 grid, the data base, code and system requirements are nearly 21 large pages. Testing has shown that each forward-reverse sweep gives only 5 large-page faults per time step, as predicted. SPECFD uses the CYBER 203 ADVISE feature to overlap the I/O time with CPU execution. The total CPU time for a 32 x 32 x 64 run is about 3.1 sec per time step.

3. Numerical Simulation of Turbulent Flow Over Wavy Walls

Introduction

A general computer code to solve the Navier-Stokes equations in two-dimensional geometries with a turbulence model has been developed. Here we report on the results for flows over wavy walls including turbulence effects by means of one- and two-equation turbulence models and compare the results with available experimental results.

In order to compute turbulent flows in complicated geometries at realistic Reynolds numbers, it is necessary to model the effects of turbulence. Perhaps the simplest model is a one-equation model in which the Reynolds stress is determined by the mean-velocity gradient in terms of a relation of the form

$$-(\overline{u_i u_j} - \frac{2}{3}\delta_{ij}k) = \nu_T \left(\frac{\partial U_i}{\partial x_j} + \frac{\partial U_j}{\partial x_i}\right)$$

where ν_T is an appropriate eddy viscosity. The eddy viscosity ν_T is then modeled in terms of a turbulent length scale L as

$$\nu_T = L^2 \left[\frac{\partial U_i}{\partial x_j}\left(\frac{\partial U_i}{\partial x_j} + \frac{\partial U_j}{\partial x_i}\right)\right]^{1/2}$$

The turbulence length scale 'L' includes effects of pressure gradients as well as other effects such as the presence of a wall. The choice of 'L' will generally involve one or more free constants C_L that must be chosen to match experimental results.

One equation turbulence models of the form (I.1) have been quite successful at modeling flows that are in equilibrium. However, the constants C_L used in the closure must be changed when the flow changes. In highly non-equilibirum flows (such as flows undergoing strong acceleration), the optimal choice of these modeling constants may be difficult, if not impossible, to achieve. Also, in flows where there is flow reversal, the utility of one-equation models is dubious.

In the last decade, there have been several attempts to improve upon the one-equation models of turbulence by means of multi-equation models. In two-equation models of k-ε type, gradient transport equations are developed for turbulent kinetic energy (k) and turbulent energy disipation (ε). Such two-equation models have been successfully applied to the calculation of flows in the presence of strong pressure gradients. There has also been some work with three- and four-equation turbulence models but the payoff for the increased computational and analytical complexity of these latter models has not yet been spectacular.

The principle drawback to the use of two-equation turbulence models is that it increases the computational complexity of the system of equations one has to solve. There is also the difficulty of having more free constants in the model than in one-equation models. It is only in the past few years that these two-equation models have been coupled with full two-dimensional Navier-Stokes codes. The present work is notable in that we present results for the time dependent Navier-Stokes equations coupled with two-equation models in complicated wavy geometries. We choose to use a modified version of the two-equation turbulence model due to Jones & Launder (1972), as modified by Chien (1980). The test results discussed below are presented for relatively low Reynolds number flows because of the special interests of these flows in applications. At low Reynolds numbers, the validity of the two-equation models is severely tested.

Method of Solution

The two dimensional Navier-Stokes equations are

$$\frac{\partial v_\alpha}{\partial t} + \vec{v}\cdot\nabla v_\alpha = -\frac{\partial p}{\partial x_\alpha} + \frac{\partial}{\partial x_\beta} T_{\alpha\beta} \qquad \text{(II.1)}$$

and

$$\nabla\cdot\vec{v} = 0 \qquad \text{(II.2)}$$

where the stress tensor T includes both viscous stresses and turbulent Reynolds stresses. Equations (II.1, 2) are solved in the region

$$0 \leq x \leq 2\pi, \quad f(x,t) \leq y < \infty \qquad \text{(II.3)}$$

above the wall $y = f(x,t)$. Periodic inflow-outflow boundary conditions are applied in x:

$$\vec{v}(x \leq 2\pi,\ y,t) = \vec{v}(x,y,t) \qquad \text{(II.4)}$$

A conformal mapping technique (Meiron, Orszag & Israeli 1981 and Sec. I) is used to transform the region in (II.3) into the region

$$0 \leq \zeta \leq 2\pi, \quad 0 \leq \eta < \infty \qquad \text{(II.5)}$$

non-conformal stretching of the η variable is used to implement the spectral methods used to solve the Navier-Stokes equations.

Eqs. (II.1 - 5) are solved by a fractional-step spectral method described in detail by Meiron, Orszag & Israeli (1981). The principle changes concern the turbulence model, which will now be described.

The turbulence model used in our calculations is that of Jones & Launder (1972), as modified by Chien (1980). The modeling equations are:

$$T_{ij} = (\nu+\nu_T) \left(\frac{\partial U_i}{\partial x_j} + \frac{\partial U_j}{\partial x_i}\right) \tag{II.6}$$

$$\frac{D\varepsilon}{Dt} = c_1 \nu_T \frac{\varepsilon}{k} \left(\frac{\partial U}{\partial y}\right)^2 - c_2 \frac{\varepsilon^2}{k} + 2\nu\frac{\varepsilon}{y^2} e^{-c_4 y+}$$

$$+ \frac{\partial}{\partial x} \left(\nu+ \frac{\nu_T}{\sigma_\varepsilon}\right) \frac{\partial \varepsilon}{\partial x} + \frac{\partial}{\partial y} \left(\nu+ \frac{\nu_T}{\sigma_\varepsilon}\right) \frac{\partial \varepsilon}{\partial y} \tag{II.7}$$

$$\frac{Dk}{Dt} = \nu_T \left(\frac{\partial U}{\partial y}\right)^2 - \varepsilon - \frac{2\nu k}{y^2}$$

$$+ \frac{\partial}{\partial x} \left(\nu + \frac{\nu_T}{\sigma_k}\right) \frac{\partial k}{\partial x} + \frac{\partial}{\partial y} \left(\nu+ \frac{\nu_T}{\sigma_k}\right) \frac{\partial k}{\partial y} \tag{II.8}$$

where the 'eddy viscosity' ν_T is given in terms of the turbulent kinetic energy k and dissipation ε by

$$\nu_T = C_\nu \frac{k^2}{\varepsilon} (1-e^{-c_3 y_+}) \qquad \text{(II.9)}$$

here the modeling constants are chosen as

$$c_1 = 1.35, \quad c_2 = c_{21}(1-c_{22}e^{-R_T^2/c_{23}})$$

$$c_{21} = 1.8, \quad c_{22} = 2/9, \quad c_{23} = 36, \quad c_4 = 0.5 \qquad \text{(II.10)}$$

$$c_\nu = 0.09, \nu = 1.57\ 10^{-4}, \quad \sigma_k = 1, \quad \sigma_\varepsilon = 1.3$$

where $R_T = k^2/\varepsilon\nu$ is a turbulent Reynolds number and the subscript $+$ indicates wall units. The remaining modeling constants c_3 is chosen <u>a posteriori</u> to achieve the best agreement between our calculations and available experimental data.

Results

In Fig. 1, we plot the skin friction distribution as calculated from flow over a flat plate with zero gradient. In this figure, we show results obtained using our spectral code with both a one equation turbulence model and a two-equation model described in Sec. II. Results are presented for the two-equation model with several choices of the modeling constant c_3. Chien (1980) suggested the choice $c_3 = 0.0115$; we find that $c_3 = 0.010$ gives better agreement with experiment.

The agreement between experiment and numerical calculation achieved in Figure 1 is noteable because of the apparently significant difference between the periodic boundary conditions employed in the computer code and the true physical inflow-outflow boundary condition. It appears that periodic boundary conditions can be used to model the true physics of these boundary layer flows with little or no distortion of the results. This conclusion is extremely important for time-dependent solutions of the Navier-Stokes equations. With inflow-outflow conditions, a large computational domain must be used to stimulate flow over a long physical body, while with periodic boundary conditions, the calculations can be done over domain of limited spacial extent.

In Figure 2, we plot the distribution of Reynolds stress (normalized by u_τ^2) as a function of the wall variable y_+ , again for a flat plate with zero pressure gradient. The agreement with the classical data of Schubauer is excellent.

In Figure 3, we plot $\varepsilon\nu/u_\tau^2$ as a function of y_+, again for a flat plate with zero pressure gradient.

In Figure 4, we again plot $\varepsilon\nu/u_\tau^2$ vs y_+, at 21 downstream locations (as determined by the transformation $x = Ut$ where U is the free-stream velocity and t is the integration time in the quasi-steady state achieved by the periodic boundary condition code). These downstream locations have Reynolds numbers R_θ varying from 2000 to 4400. Observe that the results lie on a universal (R_θ - independent) curve.

In Figure 5, we plot the kinetic energy distribution k (normalized by U_τ^2) as a function of y_+ for flow over a flat plate. The peak of k occurs at $y_+ = 25$, in good agreement with available measurements.

We have used the two-equation models together with our spectral code to study turbulent flows over wavy walls. Here we will report results only for flows over sinusoidal wavy walls:

$$y = a \sin(kx) \qquad \text{(III.1)}$$

in the runs reported below, ka = 0.078 so the ratio of amplitude to wave length, a/λ, is 0.125.

In Figure 6,7, we plot the variation of U_+ (downstream velocity in wall units) as a function of y_+ in the region of maximum adverse and favorable pressure gradient, respectively. In Figure 8, we plot the distribution of boundary layer thickness as a function of position over the wave. In agreement with experiment, the bounary layer is thickest at the tough of the wave.

In Figure 9, contours of the turbulent kinetic energy distribution k, over the wave surface are plotted. In Figure 10, a similar plot of the turbulent dissipation , ε, is made. From these Figures, it is apparent that both turbulent kinetic energy and dissipation tend to become smaller in the region of favorable pressure gradients. As the waves get steeper, this indicates the tendency for relaminarization in these regions, so there may be a serious problem with two-equation turbulence models

in regions of favorable pressure gradient induced be steep curvature.

In Figure 11, we plot contours of the pressure distribution over the wavy wall. The maximum value of the pressure coefficient C_p and the phase of the pressure distribution over the wall agree well with available experimental data correlations.

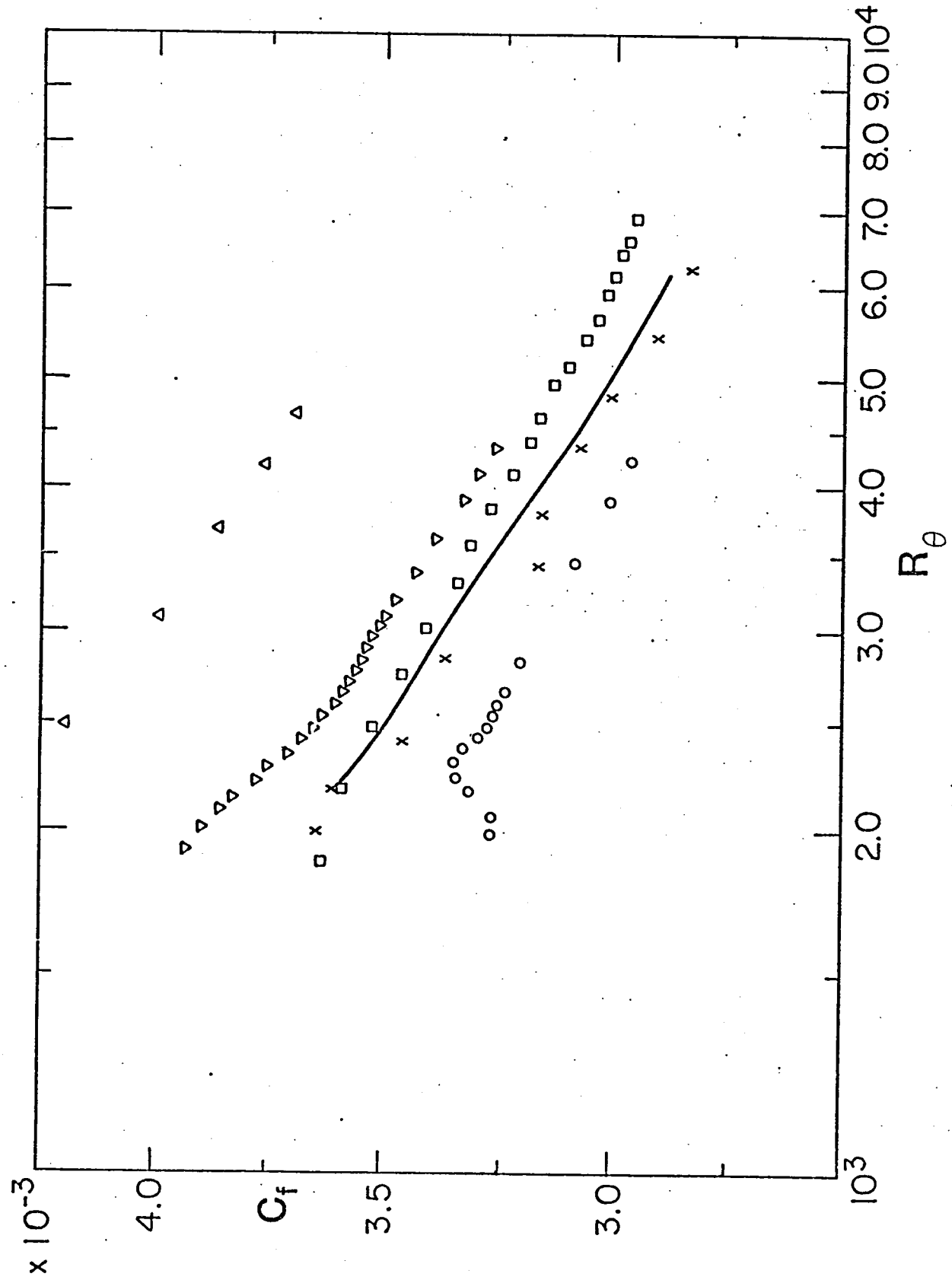

Figure 1. Variation of coefficient of skin friction for a flat plate boundary layer vs R_θ. Here the solid curve is obtained from the two-equation model (II.6)-(II.10) with $c_3 = 0.10$. The other points are: △ Model solution with $c_3 = 0.02$; ▽ Model solution with $c_3 = 0.0115$, as used by Chien; □ One equation model; ○ $c_3 = 0.008$; ╳ Experimental results due to Weighardt.

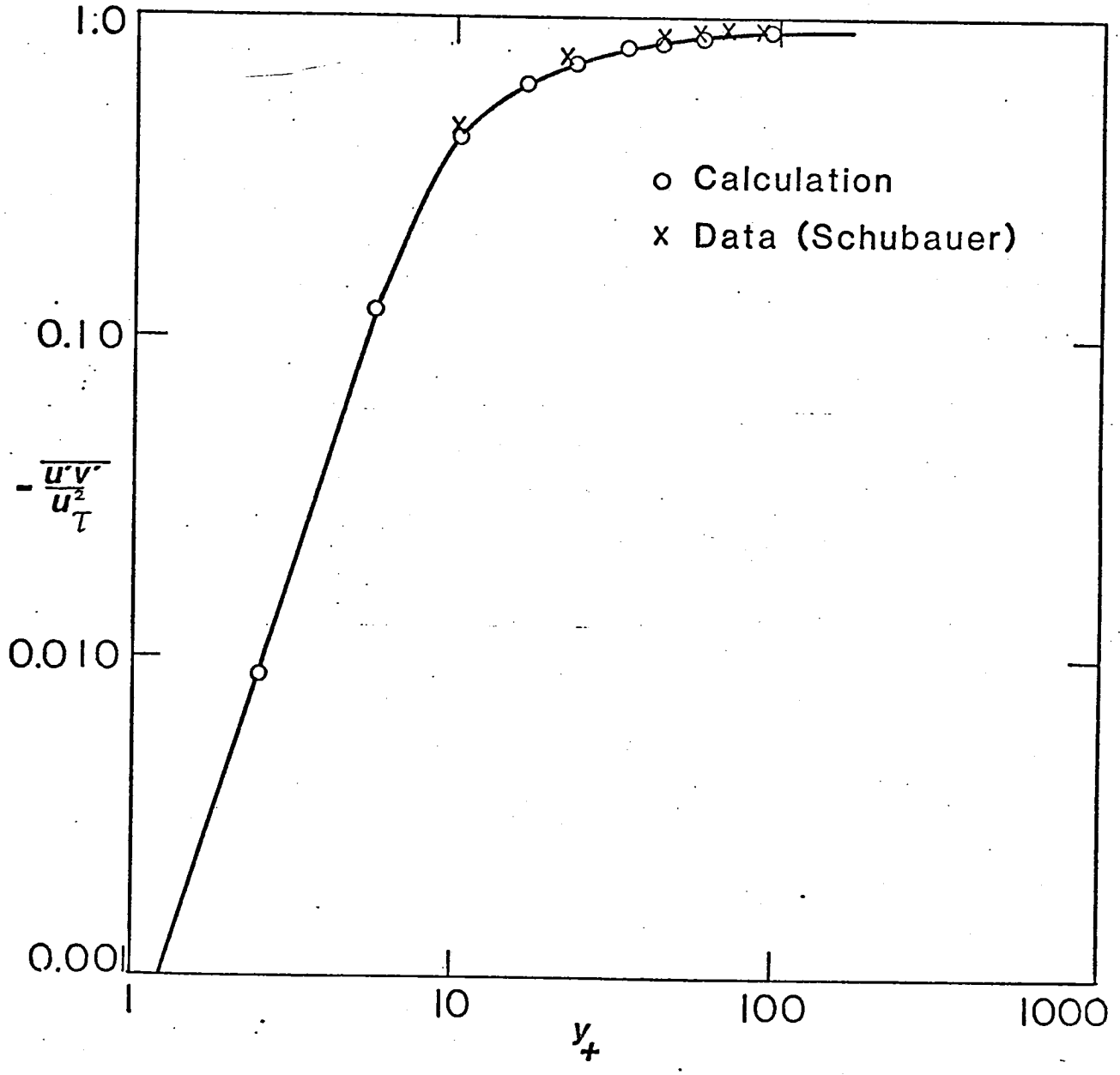

Figure 2. Variation of Reynolds stress vs y_+ for a flat plate boundary layer in zero pressure gradient.

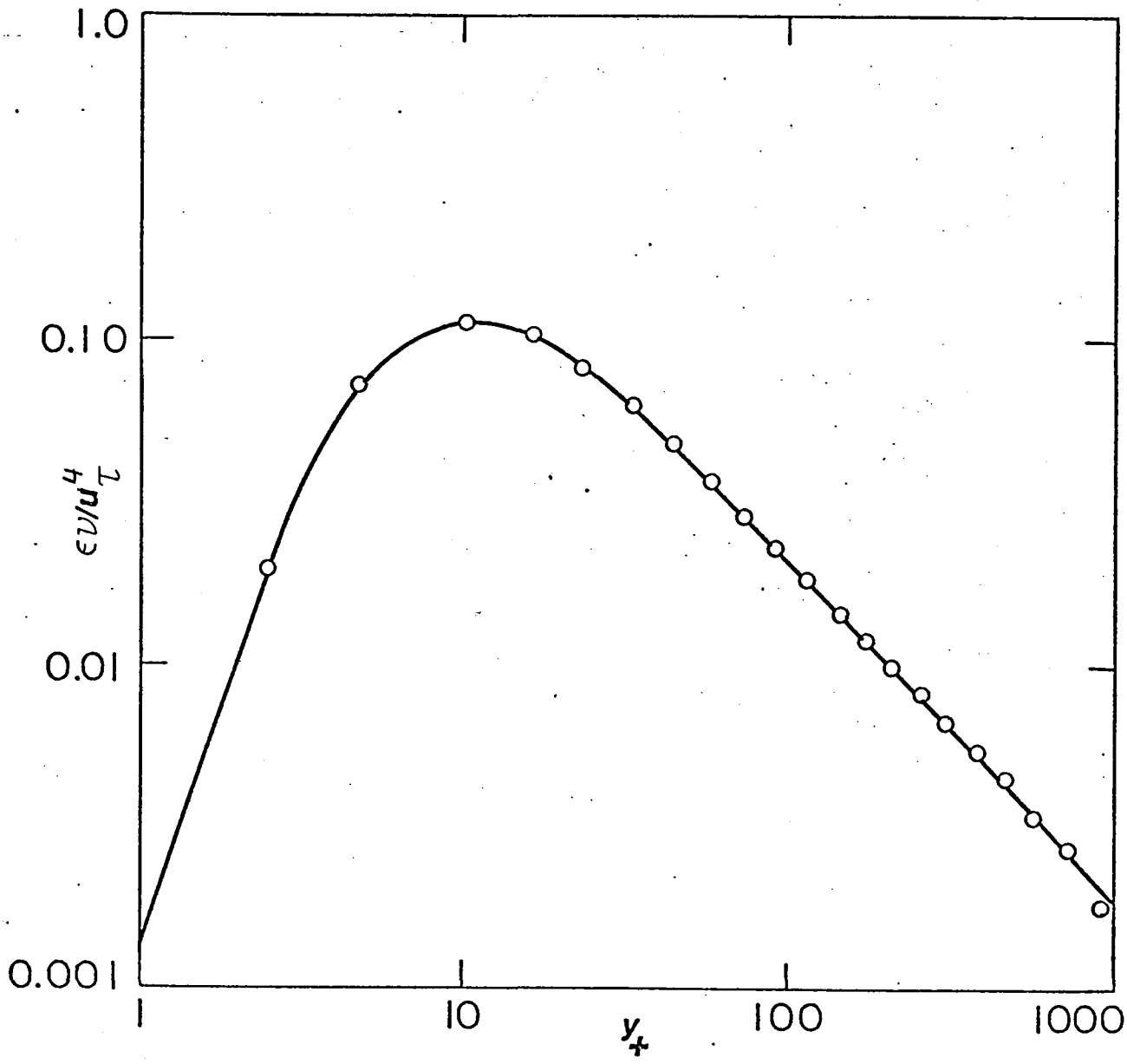

Figure 3. A plot of $\varepsilon\nu/u_\tau^4$ vs y_+ for a flat plate boundary layer in zero pressure gradient.

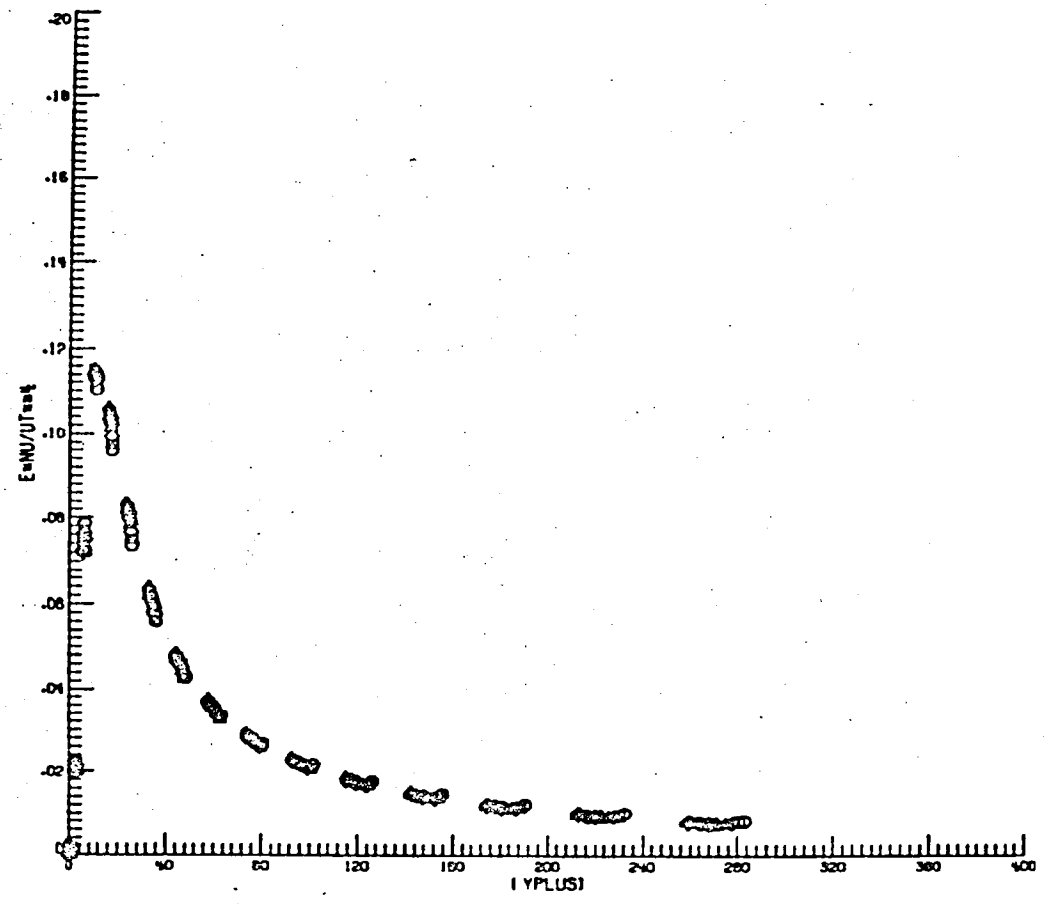

Figure 4. A plot of $\varepsilon\nu/u_\tau^4$ vs y_+ at 21 x stations with R_θ varying from 2000 to 4400. The calculations were made for a flat plate with zero pressure gradient using the two-equation model with $c_3 = 0.0115$.

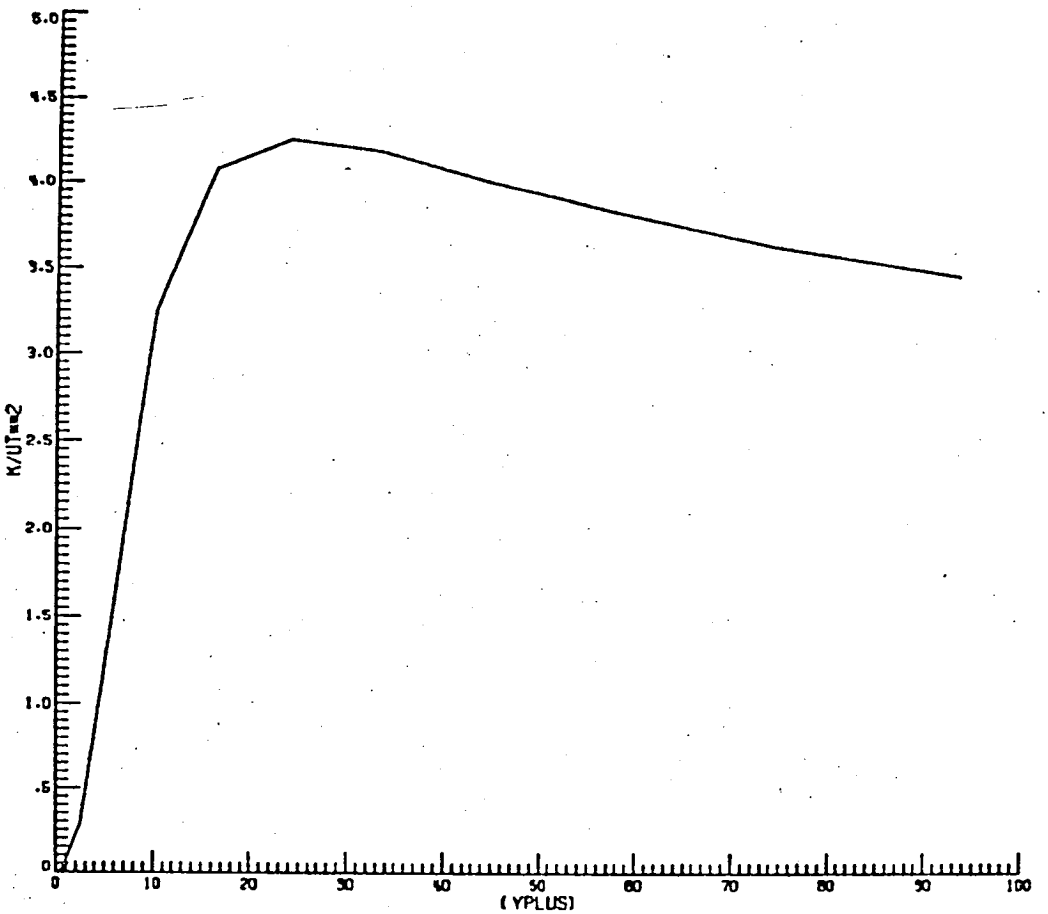

Figure 5. A plot of the kinetic energy distribution for flow over a flat plate in zero pressure gradient, as determined by the two-equation model.

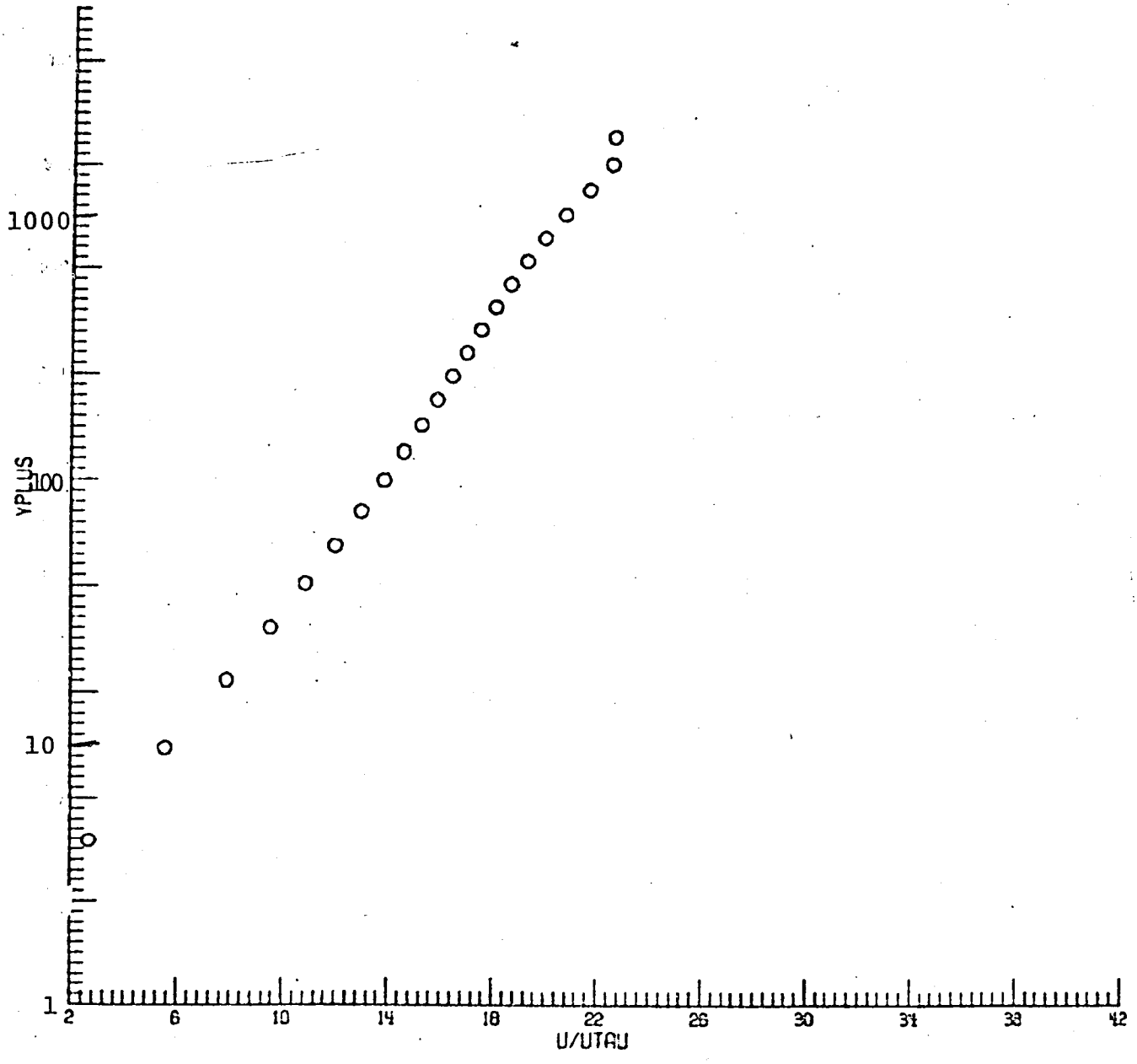

Figure 6. A plot of U_+ vs y_+ for flow over a wavy surface. The plot is made at the location of maximum favorable pressure gradient with ka = 0.0785.

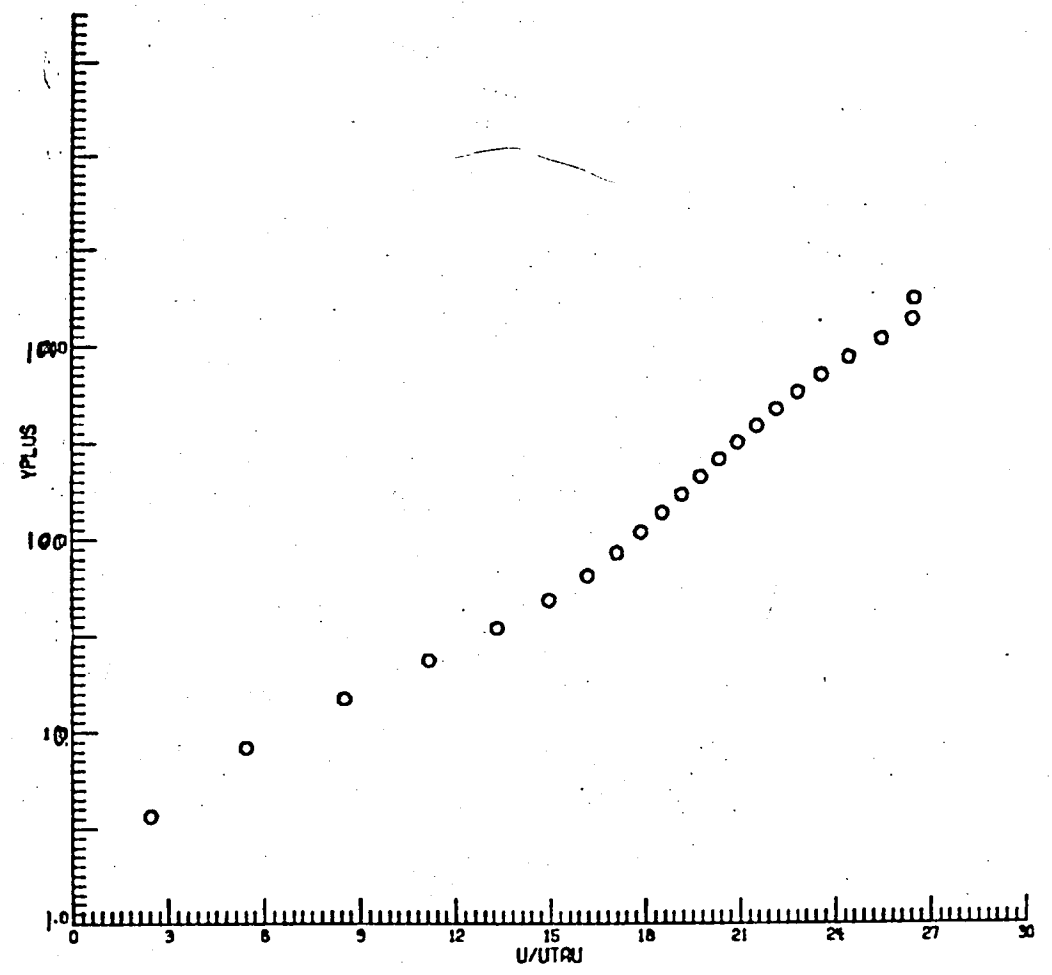

Figure 7. Same as Figure 6 except at the location of maximum adverse pressure gradient.

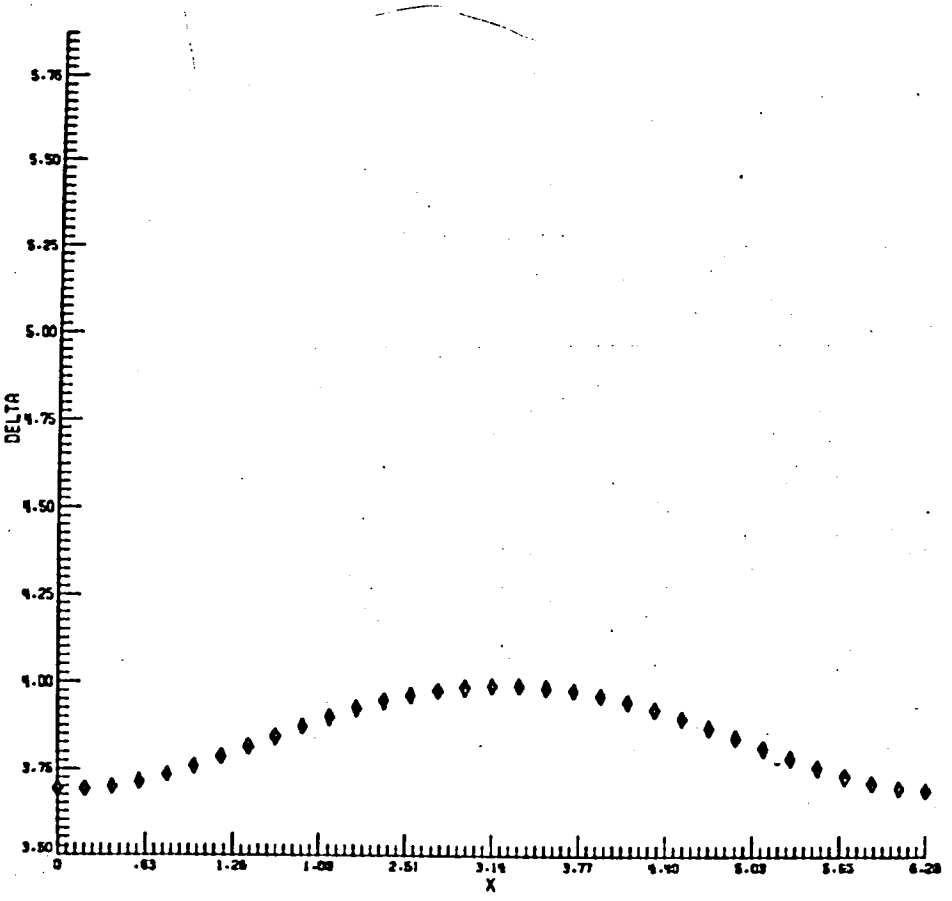

Figure 8. A plot of the boundary layer thickness as a function of x for flow over a wavy surface with ka = 0.0785. Here x = 0 corresponds to a wave crest while x = 3.14 corresponds to a wave trough.

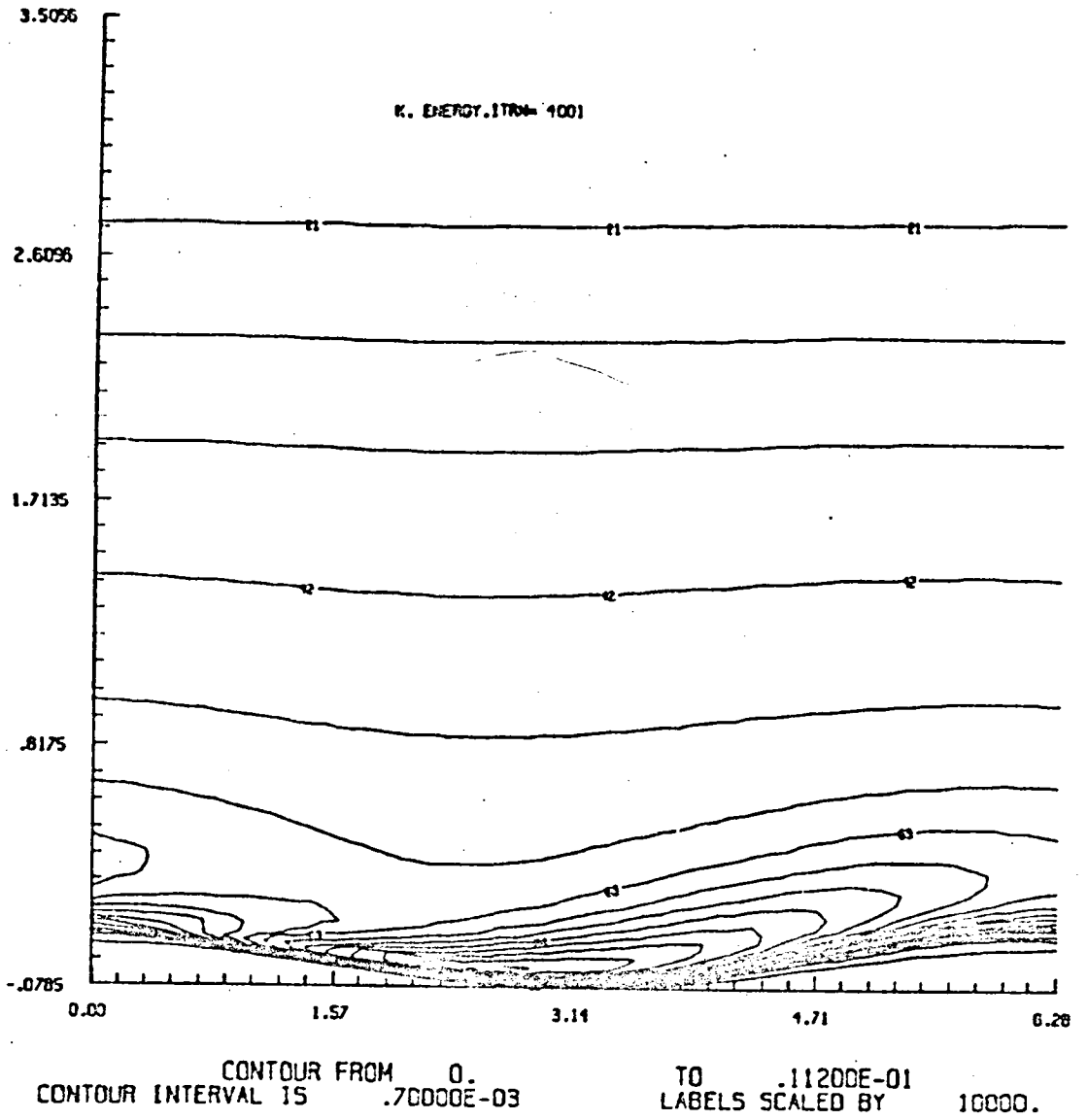

Figure 9. A contour plot of the kinetic energy distribution for flow over a wavy surface with ka = 0.0785.

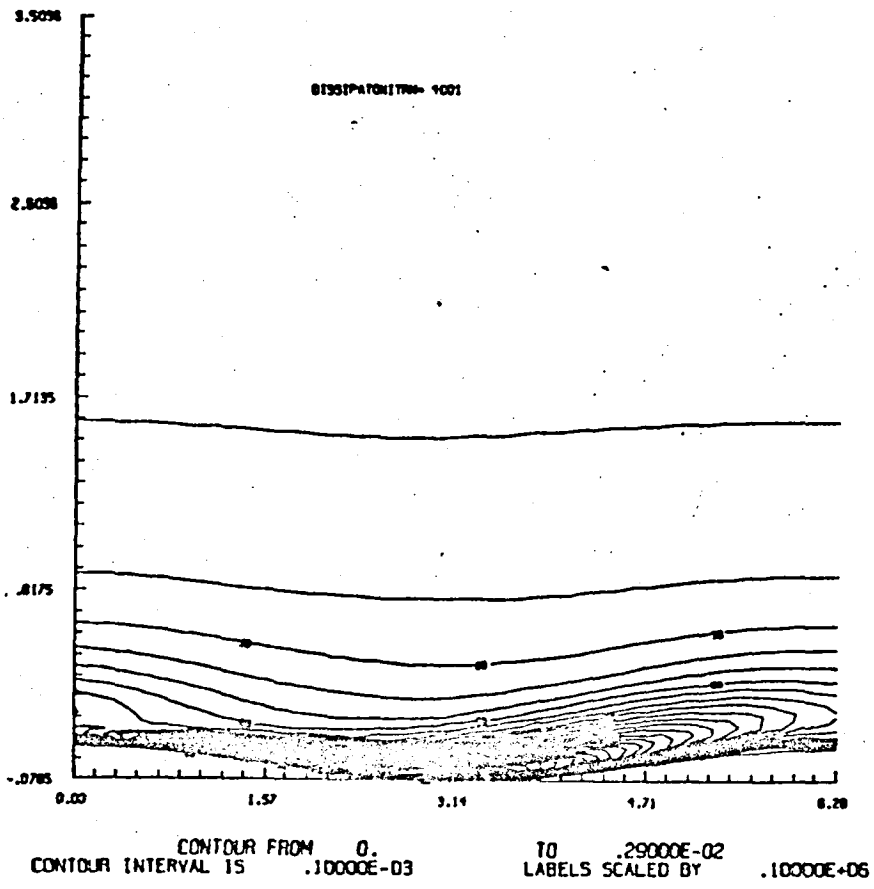

Figure 10. A contour plot of the turbulent dissipation for flow over a wavy surface with ka = 0.0785.

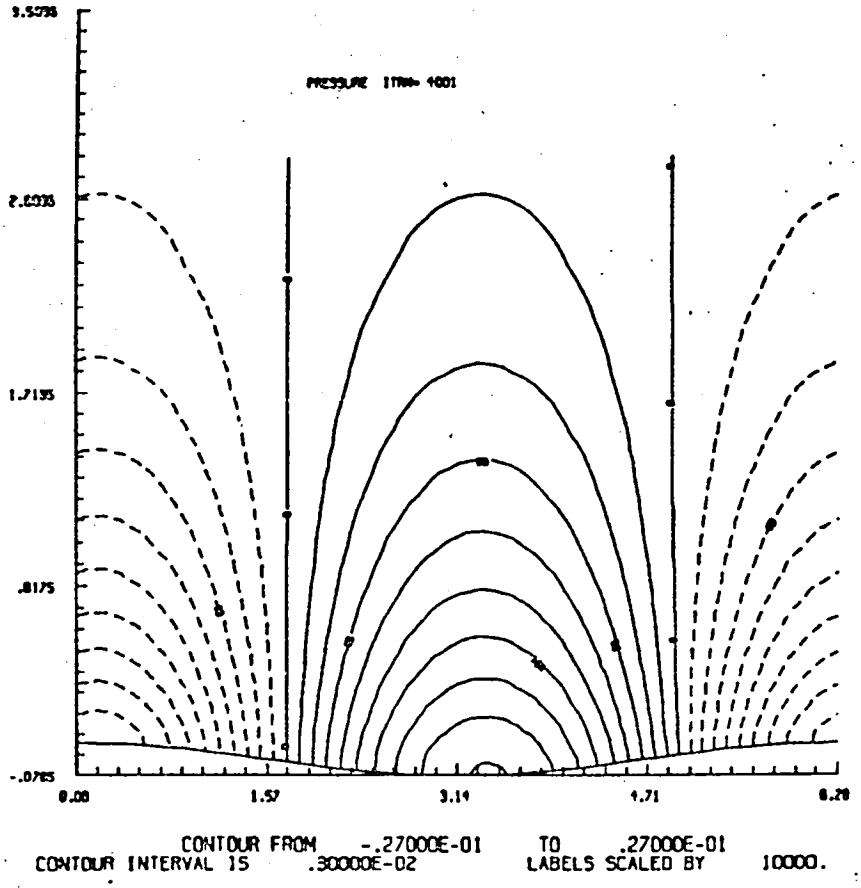

Figure 11. A contour plot of the pressure distribution for flow over a wavy surface with ka = 0.0785.

1. Report No.	2. Government Accession No.	3. Recipient's Catalog No.
NASA CR-165690		

4. Title and Subtitle	5. Report Date
Studies of Compressible Shear Flows and Turbulent Drag Reduction	April 1981
	6. Performing Organization Code
7. Author(s)	8. Performing Organization Report No.
Steven A. Orszag	CHI Report No. 49
	10. Work Unit No.
9. Performing Organization Name and Address	11. Contract or Grant No.
Cambridge Hydrodynamics, Inc. P.O. Box 249, MIT Station Cambridge, Massachusetts 02139	NAS1-15844
	13. Type of Report and Period Covered
12. Sponsoring Agency Name and Address	Final
National Aeronautics and Space Administration Washington, DC 20545	14. Sponsoring Agency Code

15. Supplementary Notes

Langley Technical Monitor: Dennis M. Bushnell

16. Abstract

Three types of problems are addressed. (i) A summary is given of recent work on the analytical and numerical aspects of conformal mapping. A new and very efficient and robust method for computation of these maps is presented. (ii) The computer code SPECFD for solution of the three-dimensional time-dependent Navier-Stokes equations for compressible flow on the CYBER 203 computer is described. Resolutions of up to 32 x 32 x 64 are possible with this code. (iii) Results of two-equation turbulence modelling of turbulent flow over wavy walls is presented. A modified Jones-Launder model is used in a two-dimensional spectral code for flow in general wavy geometries.

17. Key Words (Suggested by Author(s))	18. Distribution Statement
Conformal mapping Spectral methods Compressible flow Turbulent flow Boundary layers Turbulence model	UNLIMITED - UNCLASSIFIED

19. Security Classif. (of this report)	20. Security Classif. (of this page)	21. No. of Pages	22. Price*
Unclassified	Unclassified	61	

For sale by the National Technical Information Service, Springfield, Virginia 22161